

# Active Debris Removal (ADR): A Remedial Strategy for Sustainable Satellite Operations

Farhad Aghili<sup>a\*</sup>

<sup>a</sup> Canadian Space Agency (CSA), 6767 route de l'aéroport, St-Hubert, Quebec, J3Y 8Y9, Canada.

\* Corresponding Author

## Abstract

The growing accumulation of space debris poses a significant threat to the sustainability of satellite operations, as collisions generate thousands of hazardous fragments that further exacerbate the problem. Studies by national space agencies emphasize the urgent need for active debris removal strategies to mitigate this risk and ensure the long-term safety of space activities. This paper presents a concept for Active Debris Removal (ADR) systems that employs robotic technology to autonomously capture and dispose of large orbital debris, such as defunct satellites and spent rocket stages. The ADR system consists of a servicing satellite equipped with at least one articulated robotic arm and a capture mechanism. The targeted debris objects are assumed to be non-cooperative, i.e., lacking dedicated docking interfaces and may exhibit uncontrolled tumbling and spinning motions. The ADR system is designed to perform a sequence of key operations, including: (i) orbital maneuvers for rendezvous and proximity operations, (ii) vision-based inspection of the target, (iii) autonomous or remotely assisted rendezvous, (iv) capture and stabilization of the debris by dissipating its angular momentum, and (v) disposal of the object via transfer to a graveyard orbit or a controlled reentry trajectory. The core of the ADR system is an integrated vision-based guidance and control framework that enables autonomous robotic capture and stabilization of moving targets under complex dynamic conditions. Our approach employs an optimal control strategy for eye-to-hand visual servoing, incorporating two sequential sub-maneuvers: pre-capture synchronization with the target's motion and post-capture stabilization using an articulated robotic arm. Real-time vision-based feedback is utilized to adaptively tune control parameters, ensuring robust operation despite uncertainties in the target's dynamic behavior. The effectiveness of the proposed ADR system is validated through hardware-in-the-loop simulations using a ground-based satellite simulator testbed.

**Keywords:** active debris removal, orbital debris, space robotics, on-orbit servicing, sustainable satellite operations

## Acronyms/Abbreviations

ADR	Active Debris Removal.
IDAC	Inter-Agency Space Debris Coordination Committee.
LEO	Low Earth orbit.
SSA	Space Situational Awareness.
RAAN	Right Ascension of the Ascending Node.
CoM	Center of mass.

## Nomenclature

$\mathbf{c}_1, \dots, \mathbf{c}_m$	= Point-cloud data set output of the 3D vision sensor.
$\mathbf{r}, \rho$	= Location of the space robot end-effector and target grasping point.
$m, \mathbf{I}_c$	= The mass and inertia matrix of the space debris object.
$\mathbf{f}_e, \tau_e$	= Force and torque exerted by the space robot to the space debris object.
$\mathbf{\varrho}$	= CoM location of the debris object.
$\mathbf{q}$	= Quaternion representing the target orientation.
$\omega$	= Angular velocities of the target debris
$\sigma$	= Inertia ratio parameters of the debris object, $\sigma_1 = (I_{yy} - I_{zz})/I_{xx}$ , $\sigma_2 = (I_{zz} - I_{xx})/I_{yy}$
$\Omega_s, \Omega_d$	= RAAN of the servicing satellite and debris orbits.
$J_2$	= The second zonal harmonic of Earth's gravitational potential.
$\rho_o$	= Distance between the CoMs of the servicing satellite and target.
$[\cdot \times]$	= Matrix form of the cross-product.
$[\mathbf{n}] \otimes$	= Quaternion product.

## 1. Introduction

Even before the recent surge in satellite constellations proposed by various commercial entities, concerns about space sustainability were already mounting. A persistent challenge is the continuous accumulation of defunct satellites—particularly as historical data suggests that approximately 10% of satellites fail before reaching their planned end of life, contributing to an ever-growing population of space debris [1]. If this trend continues, the long-term sustainability of spaceflight could be at serious risk due to the increasing number of defunct satellites. A major concern in this context is the Kessler Syndrome, a phenomenon proposed by D. J. Kessler, which describes a cascading effect where collisions between space debris generate even more fragments, leading to an exponential increase in debris density. Left unmitigated, this process could ultimately render certain orbital regions unusable. Recognizing this risk, the Inter-Agency Space Debris Coordination Committee (IADC) was established and formally endorsed by the United Nations in 2008 to develop global mitigation guidelines aimed at preserving the long-term sustainability of Earth's orbital environment. However, if the current trend of satellite proliferation continues without effective debris removal and mitigation strategies, the long-term sustainability of spaceflight could be jeopardized.

Several studies have concluded that removing even a small number of large space objects annually from densely populated altitudes in Low Earth Orbit (LEO) could effectively stabilize the debris population [2]. To address this growing challenge, remediation strategies—particularly the active removal of large debris objects—are increasingly recognized as essential complements to mitigation efforts. Many major space agencies have investigated such Active Debris Removal (ADR) missions, including AnDROiD [3], DEOS [4], and ORCO [5]. A combination of passive and active mitigation techniques has been proposed to control debris growth in congested LEO regions [2]. One key approach to Active Debris Removal (ADR) involves using a space manipulator to capture large, uncontrolled targets in orbit [7, 8, 9]. Research on capture and de-orbiting technologies for non-cooperative debris can be found in [6], with various capture methods explored in [10], including ion-beam shepherding [11], gecko-inspired adhesives, polyurethane foam [12], and flexible link capture systems [13]. Moreover, other ADR remediation solutions, such as electrodynamic tethers [14], solid rocket motors [15], space tugs [16], nets [17], harpoons [18], and tentacle-like capture mechanisms [19], have been proposed, each presenting different levels of feasibility and associated risks.

Autonomous servicing robotics integrates a diverse range of advanced technologies, playing a crucial role in space operations. One of its most challenging applications is the capture of non-cooperative satellites and space debris—objects that exhibit uncontrolled translational and rotational motion, often due to attitude control system failures. Successful robotic capture consists of two critical phases: first, the space manipulator must securely capture the tumbling space object while mitigating its angular momentum, and second, it must stabilize the object before performing de-orbit maneuvers. Despite advancements in robotic servicing, achieving seamless planning and execution remains a complex challenge. Various guidance and control strategies have been explored to enable autonomous capture, including vision-based motion estimation and prediction techniques [7,8,20,21]. However, integrating both pre-capture and post-capture phases into a cohesive, adaptive control framework remains an open problem.

This work builds upon prior research [7,8,21] by integrating adaptive and optimal solutions tailored to the unique challenges of autonomous servicing for non-cooperative space objects. Specifically, the approach ensures smooth transitions between control strategies while accounting for dynamic uncertainties, physical constraints, and vision-based sensing limitations. The primary objectives are: (i) Developing a time-optimal trajectory planning framework for sequential capture and stabilization maneuvers, ensuring robust and time-sensitive execution under dynamic conditions; (ii) Implementing an adaptive control strategy to safely manage the satellite's tumbling motion and dissipate its angular momentum; (iii) Designing a real-time trajectory planner that integrates vision-based sensing feedback to dynamically adjust control actions. The robotic capture strategy relies on adaptive and dynamically consistent optimization techniques for both pre-capture and post-capture phases. It also demands robust and precise robotic operations in the challenging space environment, where uncertainties, physical constraints, and visual obstructions must be systematically managed. To achieve this, we present an adaptive and hierarchical trajectory planning framework that governs two sequential sub-maneuvers: (i) End-to-end time-optimal trajectory planning, incorporating multiple operational and physical constraints to ensure time-critical execution of autonomous operations; (ii) A self-adaptive planning approach that enables smooth transitions between pre-capture and post-capture control strategies. By incorporating real-time adjustments, compensating for dynamic uncertainties, and maintaining operational continuity despite temporary visual obstructions, the proposed system enhances the robustness and efficiency of the robotic space servicing operations. The effectiveness of the proposed vision-based robotic capture of space objects is validated through hardware-in-the-loop simulations, demonstrating its capability to safely capture and stabilize a tumbling defunct satellite while meeting multiple system requirements, ensuring readiness for subsequent de-orbiting tasks.

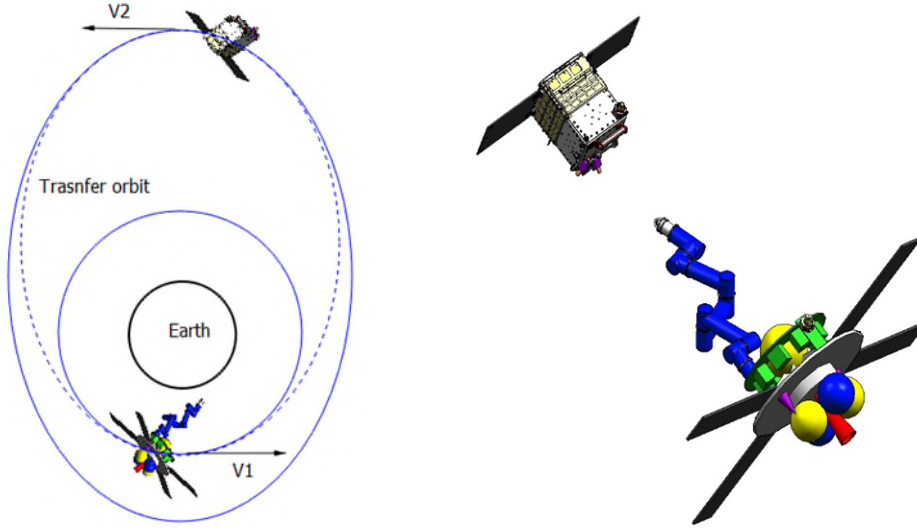


Figure 1: The orbit transfer (left) and robotic capture (right) operations in ADR.

## 2. Space Environment

The increasing proliferation of small satellites, the advancement of large-scale low Earth orbit (LEO) constellation proposals, and the continuous growth of the orbital debris population have heightened concerns regarding orbital debris risk in recent years. Environmental modeling is being employed to assess collisional probabilities, while private investment is driving the development of commercial Space Situational Awareness (SSA) and Active Debris Removal (ADR) technologies. Concurrently, industry organizations and national regulatory bodies are revising debris mitigation guidelines and licensing frameworks to address the evolving space environment. While these initiatives represent constructive responses to the growing complexities of space operations, there is a tendency to prioritize solution development before thoroughly characterizing the underlying problem. Figure 2 illustrates the exponential increase in the number of cataloged space objects, classified by orbital region, over past 60 years [23]. After more than 5,500 launches of nearly 10,000 payloads, only about 2,300 are still active today while another 3,200 remain as orbiting refuse [22, 23]. Low Earth Orbit (LEO), with an altitude of 2,000 km or lower, is the most densely populated and exhibits the highest rate of growth in cataloged objects. The distribution of cataloged objects in LEO as a function of orbital altitude, highlights a pronounced concentration of objects within specific altitude ranges, particularly between 400 km and 1,000 km, compared to other regions[22].

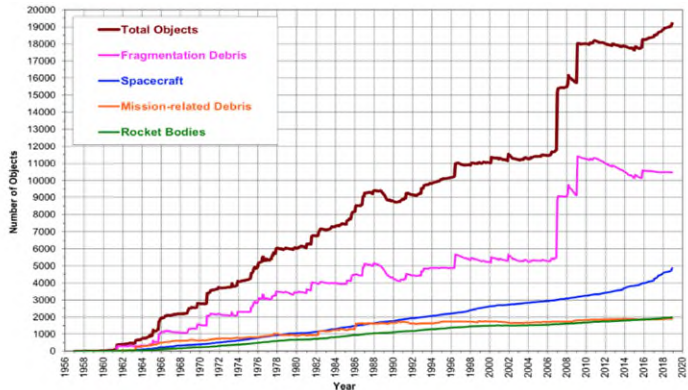


Figure 2: Evaluation of number of objects in Earth orbit [23].

As these initiatives represent constructive responses to the growing complexities of space operations, there is a tendency to prioritize solution development before thoroughly characterizing the underlying problem. Figure 2 illustrates the exponential increase in the number of cataloged space objects, classified by orbital region, over past 60 years [23]. After more than 5,500 launches of nearly 10,000 payloads, only about 2,300 are still active today while another 3,200 remain as orbiting refuse [22, 23]. Low Earth Orbit (LEO), with an altitude of 2,000 km or lower, is the most densely populated and exhibits the highest rate of growth in cataloged objects. The distribution of cataloged objects in LEO as a function of orbital altitude, highlights a pronounced concentration of objects within specific altitude ranges, particularly between 400 km and 1,000 km, compared to other regions[22].

## 2. Orbit Transfer and RAAN Alignment

As schematically shown in Figure 1, upon deployment, the ADR servicing satellite executes a multi-phase process, including: (i) orbital maneuvering and proximity operations using an advanced propulsion system, (ii) vision-based inspection of the target debris, (iii) autonomous or remotely assisted rendezvous, (iv) secure capture of the debris followed by the dissipation of its angular momentum, and (v) safe disposal by transferring it to either a designated

graveyard orbit—where it poses no risk to operational satellites—or a controlled deorbit trajectory. In addition, the ADR system has to be equipped with a self-deorbiting capability, designed to be activated either upon reaching the end of its operational life or in the event of a critical failure. To minimize the risk of accidental collisions and debris fragmentation, the ADR spacecraft should conduct a phased approach, beginning with long-range rendezvous and visual inspection, followed by controlled close-proximity maneuvers at distances of just tens of meters from the target object. The propulsion system can facilitate these maneuvers, ensuring precision and safety throughout the capture and disposal process. The system’s propulsion capability may also enable it to execute deorbit maneuver at the end of its mission life.

For the orbit transfer, it is assumed that the servicing satellite has impulsive thrust, enabling it to transition from its initial orbit to a drift orbit. The correction of the orbital parameter  $\Omega$  (Right Ascension of the Ascending Node) is achieved solely through  $J_2$  perturbation [24]. Corrections to other orbital parameters, such as the true anomaly and the argument of perigee, are neglected, as their associated transfer time and propellant consumption are considered negligible [24]. The orbit transfer can follow a two-burn strategy with an intermediate plane change: i) The first burn, a Hohmann transfer, is executed at either perigee or apogee to transfer the servicing satellite to a higher or lower orbit matching the target space object; ii) The second burn involves an inclination change maneuver performed at the node intersection of the initial and target orbits. After reaching the drift orbit, the servicing satellite remains there until its RAAN aligns with that of the space debris object.

For prediction of RAAN alignment, assume that  $i_s$  and  $i_d$  are the inclinations of the orbits of the servicing satellite in its circular drift orbit and the debris, respectively, with corresponding semi-major axes  $a_s$  and  $a_d$ . The right ascension of the ascending nodes (RAAN) of these orbits varies at the following rates [24]:

$$\dot{\Omega}_s = -\gamma a_s^{\frac{7}{2}} \cos(i_s), \quad \text{and} \quad \dot{\Omega}_d = -\frac{\gamma a_d^{\frac{7}{2}} \cos(i_d)}{(1-e_d^2)^2}, \quad (1)$$

with  $\gamma$  being a constant parameter defined as

$$\gamma = \frac{3}{2} J_2 \sqrt{\mu_e} R_e^2. \quad (2)$$

Here,  $J_2 = 1.08 \times 10^{-3}$  is the second zonal harmonic of Earth’s gravitational potential,  $R_e = 6,378,137$  m is Earth’s equatorial radius,  $\mu_e = 398,600 \text{ km}^3 \text{s}^{-2}$  is Earth’s gravitational parameter, and  $e_d$  is the eccentricity of the debris orbit. Given an initial RAAN difference  $\Delta\Omega_0$  between the two orbits, the time required for RAAN alignment can be determined from (1) as follows:

$$\Delta t = \frac{\Delta\Omega_0}{\dot{\Omega}_d - \dot{\Omega}_s}.$$

### 3. Robotic Capture and Manipulation of Space Debris Objects

As illustrated in Figure 3, the robotic capture and manipulation of space debris involves three phases: i) the learning phase, where the motion states and inertial parameters of the space object are estimated from vision data to be used in the subsequent guidance and robotic planning phase; ii) the pre-capture phase, which guides the robotic system from its home position to intercept the grasping point on the tumbling space object, taking into account environmental and system constraints; and iii) the post-capture phase, where the angular momentum of the tumbling space object is quickly damped without causing mechanical damage or actuation saturation. The following sections provide a more detailed description of these phases.

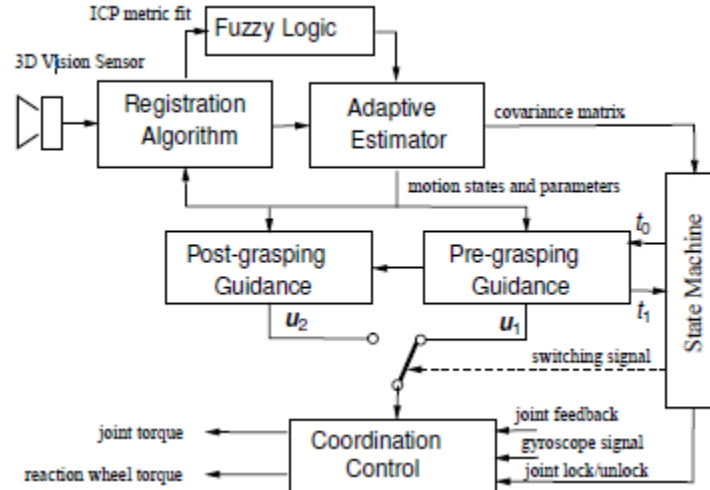


Figure 3 The GN&C block diagram for autonomous robotic capture and stabilization of a tumbling space object.

### 3.1 Modelling and Vision-Based State Estimation of Space Debris

This section presents the estimation of the motion and inertial parameters of tumbling space debris using a 3D vision sensor to support the robot's guidance and control during the pre- and post-capture phases. These phases will be discussed in more detail in the following sections. Figure 4 illustrates the coordinate frames used in a vision-guided manipulator system during the pre- and post-capture phases of a tumbling space target. The camera coordinate frame is denoted as  $\{A\}$ , while the target satellite is associated with two frames:  $\{B\}$  and  $\{C\}$ . The origin of frame  $\{B\}$  coincides with the center of mass (CoM) of the target, whereas the origin of frame  $\{C\}$  is offset by a distance  $\mathbf{q}$  from the CoM, corresponding to the location of the grasping fixture. It is assumed that frame  $\{B\}$  is aligned with the principal axes of the target. The pose (position and orientation) of frame  $\{C\}$  relative to frame  $\{A\}$  is represented by the position vector  $\mathbf{p}$  and the unit quaternion  $\mathbf{q}$ . Let  $\mathbf{\mu}$  and  $\mathbf{q}$  be the unit quaternions describing the orientations of frame  $\{C\}$  with respect to  $\{B\}$  and frame  $\{B\}$  with respect to  $\{A\}$ , respectively. Let vector  $\mathbf{c}_i \in \mathbb{R}^3$  represent the coordinate of the  $i$ th point in the point cloud acquired by the 3D vision system, see Figure 5. The instantaneous pose of the target, represented by the translation vector  $\mathbf{p}$  and quaternion  $\mathbf{q}$ , can be expressed as a function of the point cloud set:

$$\mathbf{y}(\mathbf{c}_1, \dots, \mathbf{c}_m) = \begin{bmatrix} \mathbf{p} \\ \mathbf{q} \end{bmatrix} + \mathbf{v},$$

where  $\mathbf{v}$  represents the measurement noise with covariance  $\mathbf{R} = E[\mathbf{v}\mathbf{v}^T]$ .

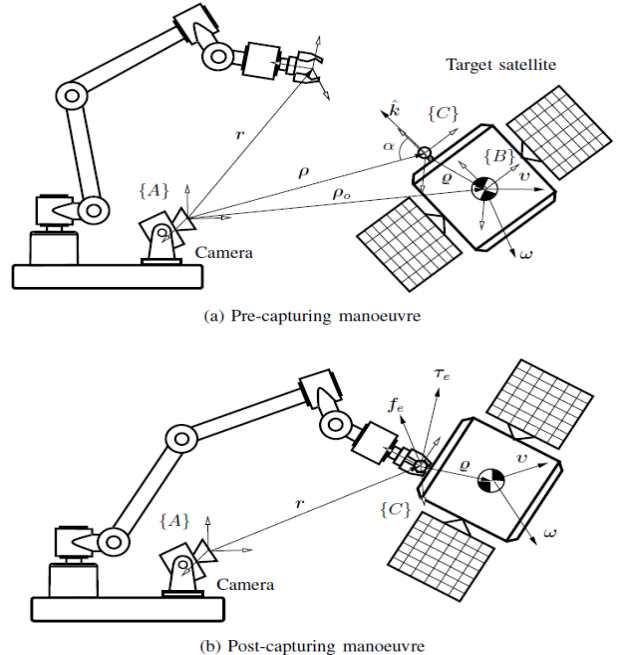


Figure 4: A servicing space robot in pre-capture and post-capture phases of a tumbling space object.

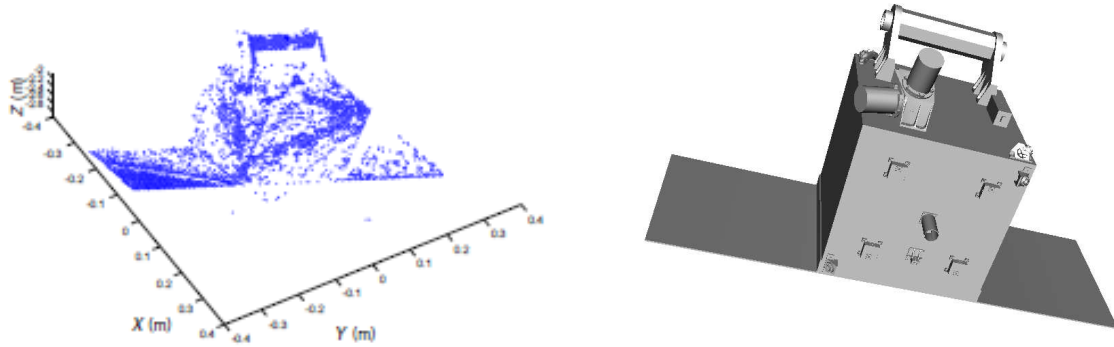


Figure 5: The set of point cloud data obtained by 3D scanning of the space target (left) and its CAD surface model (right)

Now, consider the state vector  $\mathbf{x} = [\mathbf{q}^T \ \boldsymbol{\omega}^T \ \mathbf{p}_o^T \ \dot{\mathbf{p}}_o^T \ \boldsymbol{\theta}^T]^T$ , where  $\boldsymbol{\omega}$  is the angular velocity of the space object,  $\mathbf{p}_o$  is the displacement vector representing the location of the object's CoM, and the constant vector  $\boldsymbol{\theta} = [\boldsymbol{\sigma}^T \ \boldsymbol{\varrho}^T \ \boldsymbol{\mu}^T]^T$  contains the inertial parameters to be estimated. Here,  $\boldsymbol{\sigma}$  represents the inertia ratios,  $\boldsymbol{\varrho}$  denotes the CoM location in the body frame, and quaternion  $\boldsymbol{\mu}$  describes the orientation of the object's principal axes [25]. Assuming the inertial parameters remain constant over time, we have  $\dot{\boldsymbol{\theta}} = \mathbf{0}$ . It can be shown that the system's dynamic and nonlinear observation equations for an extended Kalman estimator take the following form [25]:

$$\dot{\mathbf{x}} = \mathbf{f}(\mathbf{x}) + \mathbf{L}(\mathbf{x})\mathbf{w} \quad (3)$$

$$\mathbf{y}(\mathbf{c}_1, \dots, \mathbf{c}_m) = \mathbf{h}(\mathbf{x}) + \mathbf{v} \quad (4)$$

Here, the vector  $\mathbf{w}^T = [\mathbf{w}_\tau^T \ \mathbf{w}_f^T]^T$  represents the overall process noise with covariance matrix  $\mathbf{W} = E[\mathbf{w}\mathbf{w}^T] = \text{diag}(\sigma_\tau^2 \mathbf{I}, \sigma_f^2 \mathbf{I})$ ,  $\pi(\boldsymbol{\sigma}) = 3 + \sigma_1 \sigma_2 + \sigma_1 - \sigma_2$ ,

$$\mathbf{f}(\mathbf{x}) = \begin{bmatrix} \frac{1}{2} \text{vec}(\Lambda(\boldsymbol{\omega})\mathbf{q}) \\ \boldsymbol{\Phi}(\boldsymbol{\omega}, \boldsymbol{\sigma}) \\ \dot{\mathbf{p}}_o \\ \mathbf{0} \end{bmatrix}, \quad \mathbf{L}(\mathbf{x}) = \begin{bmatrix} \mathbf{0} & \mathbf{0} \\ \mathbf{B}(\boldsymbol{\sigma}) & \mathbf{0} \\ \mathbf{0} & \mathbf{0} \\ \mathbf{0} & \mathbf{I} \\ \mathbf{0} & \mathbf{0} \end{bmatrix}, \quad \mathbf{B}(\boldsymbol{\sigma}) = \begin{bmatrix} \frac{\pi(\boldsymbol{\sigma})}{1-\sigma_2} & 0 & 0 \\ 0 & \frac{\pi(\boldsymbol{\sigma})}{1+\sigma_1} & 0 \\ 0 & 0 & \frac{\pi(\boldsymbol{\sigma})}{1+\sigma_1\sigma_2} \end{bmatrix} \quad (5)$$

$$\mathbf{h}(\mathbf{x}) = \begin{bmatrix} \mathbf{p}_o + \mathbf{A}(\mathbf{q})\boldsymbol{\varrho} \\ \text{vec}(\boldsymbol{\mu} \otimes \mathbf{q}) \end{bmatrix}, \quad \Lambda(\boldsymbol{\omega}) = \begin{bmatrix} -[\boldsymbol{\omega} \times] & \boldsymbol{\omega} \\ -\boldsymbol{\omega}^T & 0 \end{bmatrix}, \quad \boldsymbol{\Phi}(\boldsymbol{\omega}, \boldsymbol{\sigma}) = \begin{bmatrix} \sigma_1 \omega_y \omega_z \\ \sigma_2 \omega_x \omega_z \\ -\frac{\sigma_1 + \sigma_2}{1 + \sigma_1 \sigma_2} \omega_x \omega_y \end{bmatrix}, \quad (6)$$

and  $\mathbf{A}(\mathbf{q}) = \mathbf{I} + 2q_o[\mathbf{q}_b, \times] + 2[\mathbf{q}_v, \times]^2$  is the rotation matrix corresponding to quaternion  $\mathbf{q} = [\mathbf{q}_v^T \ \mathbf{q}_o]^T$ . Using model formulation (3)-(6), a Kalman filter estimator can be developed to estimate the objects's linear and angular motion in addition to its inertial parameters [27].

### 3.2 Pre-capture Guidance and Control

This section presents the development of an optimal robotic guidance strategy for rendezvous and smooth interception of tumbling space objects using visual feedback. The end-effector position and the capture point are denoted by  $\mathbf{r}$  and  $\boldsymbol{\rho}$ , respectively. To prevent impact at the end of the capture phase, it is crucial that the robot's end-effector intercepts the target's grapple point with zero relative velocity. Assuming the optimal trajectory is governed by  $\dot{\mathbf{r}} = \mathbf{u}_1$ , this can be reformulated as  $\dot{\mathbf{x}}_1 = [\dot{\mathbf{r}}^T \ \mathbf{u}_1^T]^T$ , where  $\mathbf{x}_1^T = [\mathbf{r}^T \ \dot{\mathbf{r}}^T]$ . The objective

is to determine a time-optimal control input  $\mathbf{u}_1$  subject to acceleration constraints  $\|\ddot{\mathbf{r}}\| \leq a_{max}$  and the following terminal conditions:

$$\text{minimize} \quad \int_{t_0}^{t_1} 1 \, dt \quad (7)$$

$$\text{subject to:} \quad \|\mathbf{u}_1(\tau)\| \leq a_{1max}, \quad t_0 \leq t \leq t_1 \quad (8)$$

$$\cos^{-1}\varphi(t_1) < \alpha_{max} \quad (9)$$

$$\Psi_1(t_1) = \mathbf{0} \quad (10)$$

where

$$\Psi_1(t) = [\mathbf{r}(t) - \mathbf{p}(t)], \quad \text{and} \quad \varphi = \frac{\dot{\mathbf{p}}^T}{\|\dot{\mathbf{p}}\|} \mathbf{A}(\mathbf{q}) \mathbf{k} \quad (11)$$

Here,  $\mathbf{k}$  is the unit vector normal to the surface of the capturing fixture, and  $\alpha_{max}$  denotes the maximum line-of-sight (LOS) constraint of the target with respect to the camera, i.e., the angle between  $\mathbf{k}$  and  $\mathbf{p}$ . The terminal condition (9) ensures that the target is oriented correctly at the moment of interception to avoid LOS obstruction of the grasping point. Terminal condition (10) enforces zero relative velocity between the robot's end-effector and the tumbling space object at the instant of capture, facilitating a smooth, impact-free interception. The optimal control problem formulated in (4.2) can be solved using the Hamiltonian optimal control framework as outlined in [25,26].

### 3.3 Post-Capture Guidance and Control

In this section, we seek another optimal trajectory planning specifically for the post-capturing phase. The control objective is to damp out the momentums of the tumbling and drifting target as quickly as possible without applying excessive force and torque. Suppose the target linear velocity,  $\mathbf{v}$ , angular velocity,  $\boldsymbol{\omega}$ , as well as the exerted force,  $\mathbf{f}_e$ , and torque,  $\boldsymbol{\tau}_e$ , are all expressed in the body coordinate frame attached to the target at its location of CoM. Then, the equations of the motion of the target in the post-capturing phase is described by

$$\dot{\mathbf{v}} = -\boldsymbol{\omega} \times \mathbf{v} + \frac{1}{m} \mathbf{f}_e \quad (12)$$

$$\dot{\boldsymbol{\omega}} = \boldsymbol{\Phi}(\boldsymbol{\omega}, \boldsymbol{\sigma}) + \frac{1}{\text{tr}(\mathbf{I}_c)} \mathbf{B}(\boldsymbol{\sigma})(\boldsymbol{\tau}_e - \boldsymbol{\mathcal{Q}} \times \mathbf{f}_e). \quad (13)$$

Denoting the system states in the post-capture phase by vector  $\mathbf{x}_2^T = [\mathbf{v}^T \ \boldsymbol{\omega}^T]$  and the control input  $\mathbf{u}_2^T = [\mathbf{f}_e^T \ \boldsymbol{\tau}_e^T]$ , we are interested in optimal input trajectories  $\mathbf{u}_2^*$  which damp out the target's linear and angular velocities at the time of interception, i.e.,  $\mathbf{v}(t_1)$  and  $\boldsymbol{\omega}(t_1)$ , in minimum time subject to maximum magnitude limits of the input force and torque to be  $f_{max}$  and  $\tau_{max}$ , respectively. Note that initial linear and angular velocities of the target at the time of interception, i.e.,  $\mathbf{v}(t_1)$  and  $\boldsymbol{\omega}(t_1)$ , are equal to those the robot end-effector on the servicer and therefore they can be calculated from the robot joint rates. Thus, the otimal control in the post-capture phase can be formulated as follow:

$$\text{minimize} \quad \int_{t_1}^{t_2} dt \quad (14)$$

$$\text{subject to:} \quad \|\mathbf{f}_e\| \leq f_{max} \quad (15)$$

$$\|\boldsymbol{\tau}_e\| \leq \tau_{max} \quad (16)$$

$$\Psi_2(t_2) = \mathbf{0} \quad (17)$$

where  $\Psi_2(t) = \mathbf{x}_2(t)$  is the final condition of the post-capturing phase. The optimal control problem formulated in (12)-(17) can be solved using the Hamiltonian optimal control framework as outlined in [21].

#### 4. Validation Results from Satellite HIL Simulator

Figure 6 depicts the experimental setup of the satellite simulator, utilized to validate the proposed robotic guidance and control scheme to capture a non-cooperative space object. This scheme is designed to enable the capture and stabilization of a satellite mockup (as the space debris object) exhibiting both translational and tumbling motions, while fulfilling the functional requirements within a simulated space environment through an end-to-end robotic operation framework, encompassing learning, pre-capturing, and post-capturing phases. To simulate the dynamic behavior of a free-floating target satellite and a servicing robot, two robotic manipulator arms are employed, as illustrated in Figure 6. As shown in 7, the servicing arm is equipped with the robotic hand called SARAH (Self-Adaptive Robotic Auxiliary Hand), which was developed to adaptively grasp non-cooperative space objects [28,29]. A Neptec laser scanner, Figure 8, is positioned at a fixed location within the workspace to generate 3D image data at a 2 Hz update rate for the eye-to-hand visual servoing. The end-effector of one of the manipulator arms is mechanically attached to the satellite mockup, thereby replicating the representative motion trajectories of the target satellite. The user-defined parameters for the optimal control of both pre- and post-capturing maneuvers are  $f_{max} = 7.0 \text{ N}$  and  $\tau_{max} = 8.0 \text{ Nm}$ , and  $a_{max} = 0.1 \text{ m/s}^2$ . The target's pose, comprising position and orientation, is estimated via image processing. These estimated values are incorporated into the trajectory planning for both pre- and post-capturing phases, emphasizing the criticality of their accurate estimation for successful implementation of the guidance and control strategy. The convergence of the estimator during the learning phase is determined by continuously monitoring the Euclidean norm of the covariance matrix.

Figure 9 illustrates the estimated inertial parameters of the target derived from vision data. The motion planner continuously updates the robot's trajectories based on the latest state and parameter estimates until the vision system is occluded by the approaching robotic arm just before grasping. If the vision system fails, state and parameter estimation ceases due to the lack of reliable visual data. However, motion estimation can still provide accurate predictions of the target's pose and velocity for a few seconds during the occlusion [26]. Figures 10 and 11 depict the position and velocity trajectories of the grasping fixture relative to the end-effector during the pre-capture and post-capture phases. The plots in the figure indicate that the robot successfully captured the grasping fixture on the moving target at  $t = 121.4 \text{ s}$  and subsequently stabilized its linear and angular motions at  $t = 144.3 \text{ s}$ . The capture process was smooth, with both the end-effector and the grasping fixture reaching the interception point with matching velocities. The post-capturing maneuvers effectively attenuated both translational and rotational motion of the target satellite within 22.9 seconds, while adhering to the maximum acceleration constraints of the servicing manipulator. Figure 12 shows the time history of the force and torque applied by the manipulator's end-effector to the target, both of which remain within the prescribed maximum limits, represented by the dotted lines in the figure. In summary, the optimal trajectory planning and control strategy enables

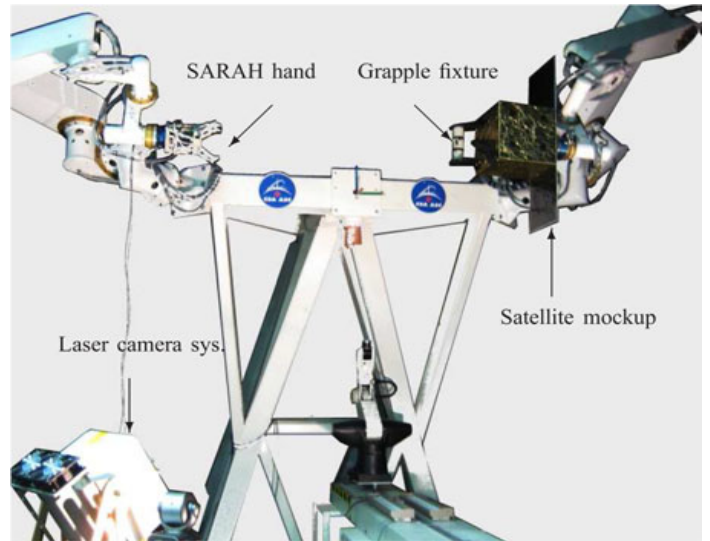


Figure 6: Experimental validation for robotic capture of a tumbling space object in hardware-in-loop simulation setting.

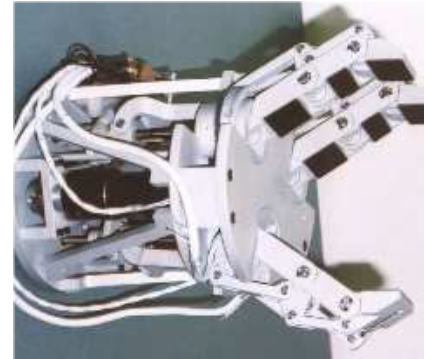


Figure 7: The robotic hand - SARAH.



Figure 8: Neptec's Laser camera system .

the robotic manipulator to capture and stabilize the target within a total execution time of 46.9 seconds, given the constraints of the manipulator's capabilities.

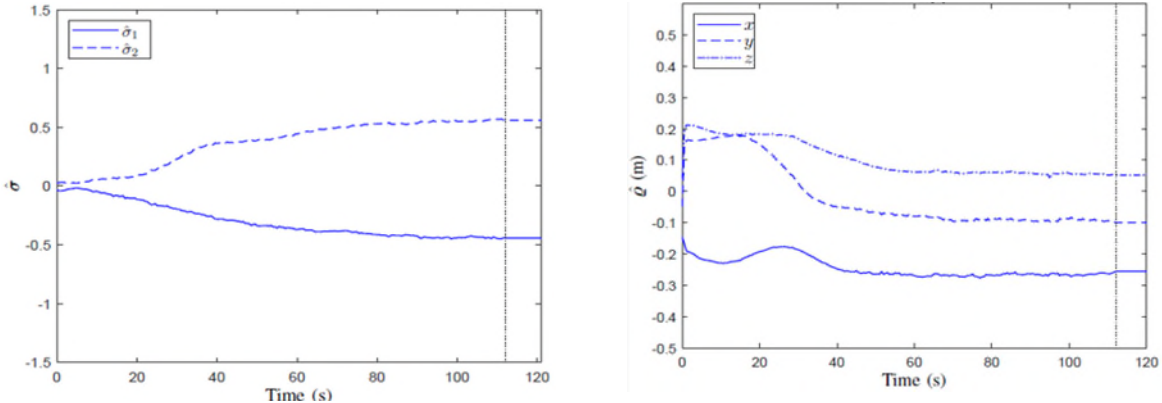


Figure 6: Estimated inertial parameters of the space object.

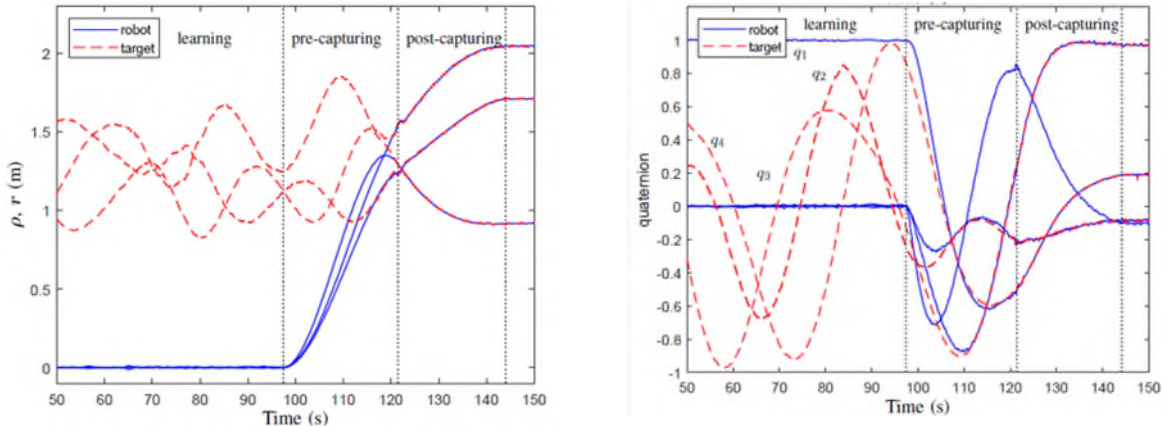


Figure 7: Positions and orientations of the robot EE versus the space object.

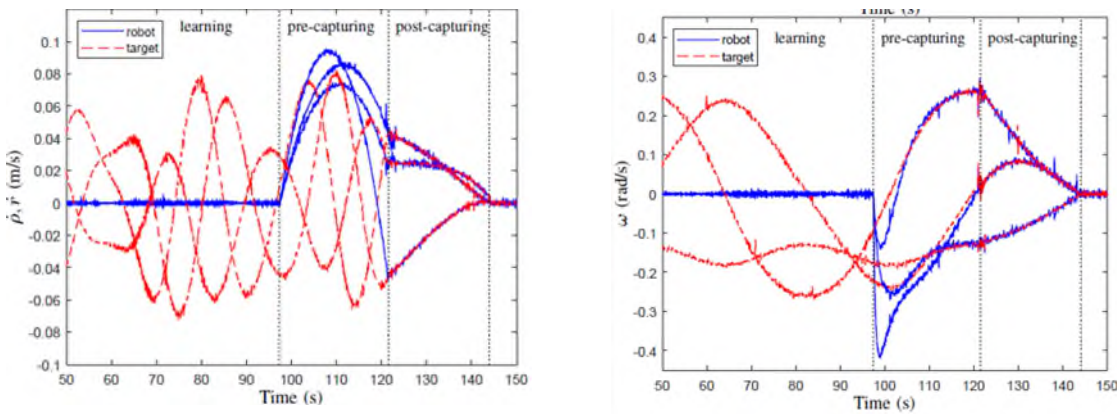


Figure 8: The linear and angular velocities of the robot EE and the space object.

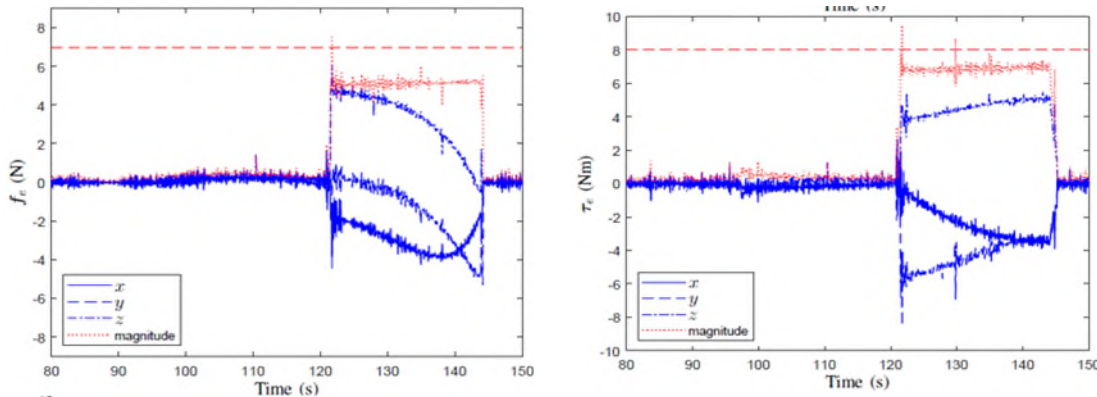


Figure 9: The contact forces and moments during detumbling of the space object.

## 5. Conclusions

This study proposed a robotic Active Debris Removal (ADR) system capable of autonomously capturing and disposing of large, non-cooperative orbital debris, such as defunct satellites and spent rocket stages. The system integrates an advanced articulated robotic arm with a vision-based guidance and control framework to enable precise debris capture, stabilization, and disposal. It is designed to perform critical operations, including orbital maneuvering, robotic capture, and stabilization for controlled debris removal, either through deorbiting or transfer to a graveyard orbit. The autonomous robotic system employs an optimal control strategy for eye-to-hand visual servoing, optimizing both pre-capture and post-capture maneuvers to ensure safe and efficient debris removal. The effectiveness of the proposed ADR system was validated through hardware-in-the-loop simulations using a ground-based satellite simulator testbed. Results demonstrated that the guidance and control strategy successfully enabled the robotic manipulator to capture and stabilize a tumbling space object within a total execution time of 46.9 seconds, while operating within the constraints of the manipulator's capabilities.

## References

- [1] A. M. Long, M. G. Richards, and D. E. Hastings, "On-orbit servicing: a new value proposition for satellite design and operation," *Journal of Spacecraft and Rockets*, vol. 44, no. 4, pp. 964–976, 2007.
- [2] G. Borelli, G. Gaias, and C. Colombo, "Rendezvous and proximity operations design of an active debris removal service to a large constellation fleet," *Acta Astronautica*, vol. 205, pp. 33–46, 2023.
- [3] D. E. Olmos, I. Newton, T. V. Peters, J. Naudet, C. Chitu, and K. Seweryn, "Android small active debris removal mission," in *Small Satellites Systems and Services - The 4S Symposium*, Majorca, Spain, 2015.
- [4] D. Reintsema, J. Thaeter, A. Rathke, W. Naumann, P. Rank, and J. Sommer, "DEOS—the German robotics approach to secure and de-orbit malfunctioned satellites from low earth orbits," in *Proceedings of the i-SAIRAS*, 2010, pp. 244–251.
- [5] P. Colmenarejo, M. Graziano, G. Novelli, D. Mora, P. Serra, A. Tomassini, K. Seweryn, G. Prisco, and J. G. Fernandez, "On ground validation of debris removal technologies," *Acta Astronautica*, vol. 158, pp. 206–219, 2019.
- [6] A. Chiesa, F. Fossati, G. Gambacciani, and E. Pensavalle, "Enabling technologies for active space debris removal: the cadet project," in *Space Safety is No Accident: The 7th IAASS Conference*. 1em plus 0.5em minus 0.4em Springer, 2015, pp. 29–38.
- [7] F. Aghili, "Optimal control for robotic capturing and passivation of a tumbling satellite with unknown dynamics," in *AIAA Guidance, Navigation and Control Conference*, Honolulu, Hawaii, August 2008, pp. 1–21.
- [8] F. Aghili, "A prediction and motion-planning scheme for visually guided robotic capturing of free-floating tumbling objects with uncertain dynamics," *IEEE Transactions on Robotics*, vol. 28, no. 3, pp. 634–649, June 2012.
- [9] K. Seweryn, F. L. Basmadjian, and T. Rybus, "Space robot performance during tangent capture of an uncontrolled target satellite," *The Journal of the Astronautical Sciences*, vol. 69, pp. 1017 – 1047, 2022.
- [10] J. Forshaw, G. Aglietti, S. Fellowes, T. Salmon, I. Retat, A. Hall, T. Chabot, A. Pisseloup, D. Tye, C. Bernal, F. Chaumette, A. Pollini, and W. Steyn, "The active space debris removal mission Remove Debris. Part 1: from concept to launch," *Acta Astronautica*, vol. 168, pp. 293–309, Mar. 2020.

- [11] E. Ahedo, M. Merino, C. Bombardelli, H. Urrutxua, J. Pelaez, and L. Summerer, "Space debris removal with an ion beam shepherd satellite: target-plasma interaction," in *47th AIAA/ASME/SAE/ASEE Joint Propulsion Conference & Exhibit*, 2011, p. 6142.
- [12] C. Trentlage and E. Stoll, "The applicability of gecko adhesives in a docking mechanism for active debris removal missions," in *13th Symposium on Advanced Space Technologies in Robotics and Automation, ASTRA*, 2015.
- [13] M. Bicocca, "Debris capture technologies overview," Tech. rep., Aviospace, Tech. Rep., 2014.
- [14] Y. Ishige, S. Kawamoto, and S. Kibe, "Study on electrodynamic tether system for space debris removal," *Acta Astronautica*, vol. 55, no. 11, pp. 917–929, 2004.
- [15] A. Okninski, "Solid rocket propulsion technology for de-orbiting spacecraft," *Chinese Journal of Aeronautics*, vol. 35, no. 3, pp. 128–154, 2022.
- [16] V. Aslanov and V. Yudintsev, "Dynamics of large space debris removal using tethered space tug," *Acta Astronautica*, vol. 91, pp. 149–156, 2013.
- [17] K. Ota and M. Takahashi, "Release of space debris from flexible nets for active debris removal," in *AIAA SCITECH 2025 Forum*, Jan 2025.
- [18] R. Dudziak, S. Tuttle, and S. Barraclough, "Harpoon technology development for the active removal of space debris," *Advances in Space Research*, vol. 56, no. 3, pp. 509–527, 2015, advances in Asteroid and Space Debris Science and Technology - Part 1.
- [19] M. Wilde, I. Walker, S. K. Choon, and J. Near, "Using tentacle robots for capturing non-cooperative space debris - a proof of concept," in *AIAA SPACE and Astronautics Forum and Exposition*, Sep 2017.
- [20] T. Rybus, K. Seweryn, and J. Z. Sasiadek, "Optimal detumbling of defunct spacecraft using space robots," in *2014 19th International Conference on Methods and Models in Automation and Robotics (MMAR)*, Sep. 2014, pp. 64–69.
- [21] F. Aghili, "Optimal trajectories and robot control for detumbling a non-cooperative satellite," *AIAA Journal of Guidance, Control, and Dynamics*, vol. 43, no. 5, pp. 981–988, 2020.
- [22] T. Maclay and D. McKnight, "Space environment management: Framing the objective and setting priorities for controlling orbital debris risk," *Journal of Space Safety Engineering*, vol. 8, no. 1, pp. 93–97, 2021.
- [23] P. D. Anz-Meador, "Orbital debris quarterly news," *NASA Orbital Debris Program Office*, vol. 23, no. 1-2, p. 13, May 2019.
- [24] N. Berend and X. Olive, "Bi-objective optimization of a multiple-target active debris removal mission," *Acta Astronautica*, vol. 122, pp. 324–335, 2016.
- [25] F. Aghili, "Autonomous sequential submanoeuvres in pre- and post-capturing space objects using obstructed 3-d vision data," *IEEE Transactions on Aerospace and Electronic Systems*, vol. 59, no. 6, pp. 7626–7639, 2023.
- [26] F. Aghili, "Fault-tolerant and adaptive visual servoing for capturing moving objects," *IEEE/ASME Transactions on Mechatronics*, vol. 27, no. 3, pp. 1773–1783, 2022.
- [27] F. Aghili and K. Parsa, "Motion and parameter estimation of space objects using laser-vision data," *AIAA Journal of Guidance, Control, and Dynamics*, vol. 32, no. 2, pp. 538–550, March 2009.
- [28] T. Laliberté and C. M. Gosselin, "Underactuation in Space Robotic Hands", Proceedings of the 6th *International Symposium on Artificial Intelligence, Robotics and Automation in Space (i-SAIRAS)*, Montreal, Canada, 2001.
- [29] B. Rubinger, M. Brousseau, J. Lymer, C. M. Gosselin, T. Laliberté and J.-C. Piedboeuf, "A Novel Robotic Hand—SARAH—for Operations on the International Space Station", Proceedings of the 7th *ESA Workshop on Advanced Space Technologies for Robotics and Automation (ASTRA 2002)*, Noordwijk, The Netherlands, November 2002.